# Raman Fingerprint of Pressure-Induced Phase Transitions in $TiS_3$ Nanoribbons Implications for Thermal Measurements under Extreme Stress Conditions

Mishra, K. K.; Ravindran, T. R.; Island, Joshua O.; Flores, Eduardo; Ares, Jose Ramon; Sanchez, Carlos; Ferrer, Isabel J.; Van Der Zant, Herre S.J.; Castellanos-Gomez, Andres; More Authors

**DOI**
10.1021/acsanm.0c01583

**Publication date**
2020

**Document Version**
Final published version

**Published in**
ACS Applied Nano Materials

ACS APPLIED NANO MATERIALS

www.acsanm.org Article

# Raman Fingerprint of Pressure-Induced Phase Transitions in $TiS_3$ Nanoribbons: Implications for Thermal Measurements under Extreme Stress Conditions

K. K. Mishra, T. R. Ravindran, Joshua O. Island, Eduardo Flores, Jose Ramon Ares, Carlos Sanchez, Isabel J. Ferrer, Herre S. J. van der Zant, Amit Pawbake, R. Kanawade, Andres Castellanos-Gomez, and Dattatray J. Late*

Cite This: *ACS Appl. Nano Mater.* 2020, 3, 8794−8802 Read Online

ACCESS | Metrics & More | Article Recommendations

**ABSTRACT:** Two-dimensional layered trichalcogenide materials have recently attracted the attention of the scientific community because of their robust mechanical and thermal properties and applications in opto- and nanoelectronics devices. We report the pressure dependence of out-of-plane $A_g$ Raman modes in high quality few-layer titanium trisulfide ($TiS_3$) nanoribbons grown using a direct solid−gas reaction method and infer their cross-plane thermal expansion coefficient. Both mechanical stability and thermal properties of the $TiS_3$ nanoribbons are elucidated by using phonon-spectrum analyses. Raman spectroscopic studies at high pressure (up to 34 GPa) using a diamond anvil cell identify four prominent $A_g$ Raman bands; a band at 557 $cm^{-1}$ softens under compression, and others at 175, 300, and 370 $cm^{-1}$ show normal hardening. Anomalies in phonon mode frequencies and excessive broadening in line width of the soft phonon about 13 GPa are attributed to the possible onset of a reversible structural transition. A complete structural phase transition at 43 GPa is inferred from the Ag soft mode frequency (557 $cm^{-1}$) versus pressure extrapolation curve, consistent with recently reported theoretical predictions. Using the experimental mode Grüneisen parameters $\gamma_i$ of Raman modes, we estimated the cross-plane thermal expansion coefficient $C_v$ of the $TiS_3$ nanoribbons at ambient phase to be $1.321 \times 10^{-6}$ $K^{-1}$. The observed results are expected to be useful in calibration and performance of next-generation nanoelectronics and optical devices under extreme stress conditions.

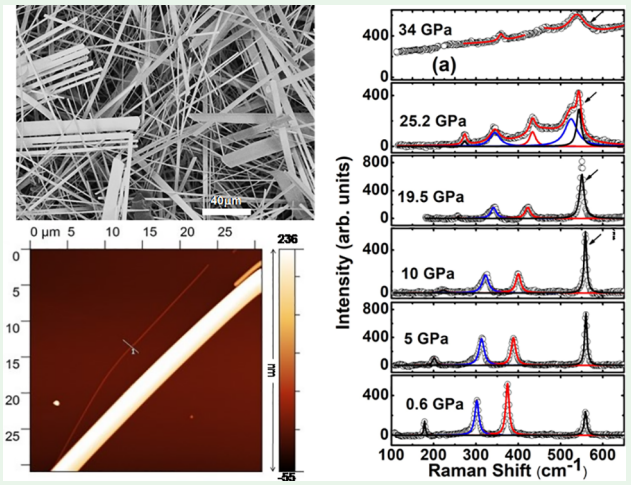


**KEYWORDS:** *$TiS_3$, high pressure, Raman spectroscopy, phonons, 2D semiconductors*



## INTRODUCTION

Two-dimensional (2D) van der Waals thin layer structure materials such as $MoS_2$, $WS_2$, $WSe_2$, $MoSe_2$, GaS, GaSe, h-BN, $SnSe_2$, $TiS_3$, GeTe, $MoTe_2$, $WTe_2$, and black phosphorus have attracted significant research interest because of their extraordinary physical, optical, and electronic properties.[1−7] These materials are found to be suitable for a wide range of applications such as gas sensors,[3,8,9] photodetectors,[10−15] transistors,[12,16−20] solar cells,[21,22] energy storage devices,[23] and field emitters.[13,24−27] The central feature of this 2D class of materials is their finite band gap unlike in graphene, which exhibits zero band gap at the Dirac K-point of the Brillouin zone and larger charge carrier mobility. These 2D materials are considered to be possible alternatives to graphene, and this has invigorated research interest in these materials.[6] Among these 2D materials, metal trichalcogenide titanium trisulfide ($TiS_3$), a direct band gap material ($E_g \sim 1$ eV) with stable layered structure, exhibits in-plane anisotropic geometry.[28−34] As a result, it shows remarkable photoresponse, gate tunability, robust thermoelectric performance, and strong quasi-one-dimensional physical properties.[32,33] *Ab initio* calculations predict anisotropic carrier mobility of a single-layer $TiS_3$[32,33] with larger carrier mobility along the *b*-axis ($13.87 \times 10^3$ $cm^2$ $V^{-1}$ $s^{-1}$), and that along the *a*-axis is relatively marginal ($1.01 \times 10^3$ $cm^2$ $V^{-1}$ $s^{-1}$). The reported carrier mobility in the $TiS_3$

**Received:** June 9, 2020
**Accepted:** August 20, 2020
**Published:** August 20, 2020

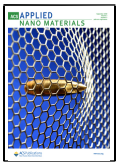

nanosheet[32] along the "*b*"- and "*a*"-axes are 80 and 40 $cm^2 V^{-1} s^{-1}$, respectively. Interestingly, the $TiS_3$ nanoribbon is found to possess superior optical tunability as compared to that of nanosheets.[32] The $TiS_3$ stabilizes in a monoclinic structure with space group $C_{2h}^2(P2_1/m)$ with two formula units per unit cell ($Z = 2$).[31] The crystal structure of a monolayer $TiS_3$ is depicted in Figure 1. The Ti−S bond length along the *b*-axis (0.245 nm) is shorter than the bond along the *a*-axis (0.265 nm)[34] which results in its in-plane anisotropic geometry. The metal ions Ti are located at the center of distorted trigonal prisms, and these trigonal faces of prism are connected to form a chain along the *b*-axis (Figure 1a). These covalently bonded parallel chains form a sheet, and such sheets are held together by van der Waals force. Hence, the $TiS_3$ crystal can be viewed as a set of stacked parallel sheets with each sheet being composed of 1D chains of a triangular $TiS_3$ unit.[32] Two kinds of sulfur atoms are seen in the structure of $TiS_3$: bridge sulfur and sulfur−sulfur pair atoms (Figure 1b).

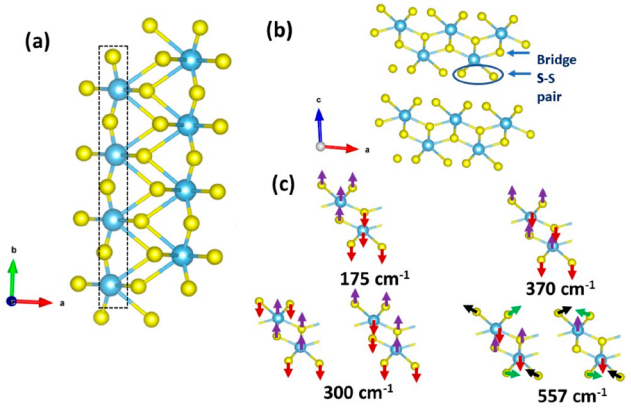


**Figure 1.** Crystal structure of titanium trisulfide. The central Ti metal atoms (light blue color) are covalently bonded to six S atoms (yellow color), forming a trigonal prism. These prisms share triangular faces to form 1D chains (shown by dashed lines). The black dashed lines mark the Ti chain along crystallographic *b*-axis. (b) Cross-sectional view of the structure of $TiS_3$, with bridge sulfur and sulfur−sulfur pair atoms. (c) Schematic representation of the motion of atoms for different pressure-sensitive Raman-active phonon modes. The bands at 300 and 557 $cm^{-1}$ are degenerate. Structure models are made by using VESTA.[55]

Although 2D anisotropic materials such as $TiS_3$ are of great practical importance,[35−38] investigations of the effect of pressure on $TiS_3$ materials are still scarce. Structural study of 2D materials subjected to pressure in a diamond anvil cell is an effective way to tune their structure[39] and electronic[40] properties. Besides, Raman spectroscopic studies on such layer materials can be useful to estimate their thermal transport properties.[39,40] Interestingly, the mechanical strain in graphene[41] and $MoS_2$[40] are reported to alter their electronic structure. $TiS_3$ exhibits a strong Raman signal[30,34] as in graphene[39] and $MoS_2$;[40] hence, Raman spectroscopy is expected to give useful insight about its structural along with mechanical stability and thermal transport properties. Raman studies[39,41] on seven-layer graphene nanosheets up to 40 GPa indicate a change in G-band slope, and its excessive broadening above 16 GPa is attributed to its deviation from 2D-layer structure. The pressure-induced isostructural electronic transition in multilayered $MoS_2$ from a semiconducting to a metallic state at 19 GPa has been inferred from high-pressure (HP) Raman spectroscopy.[40] The out-of-plane $A_{1g}$ Raman mode is an intense band that is sensitive to the electronic transition.[40] HP Raman spectroscopic studies on a $TiS_3$ whisker of ∼100 $\mu$m thickness suggested no phase transition

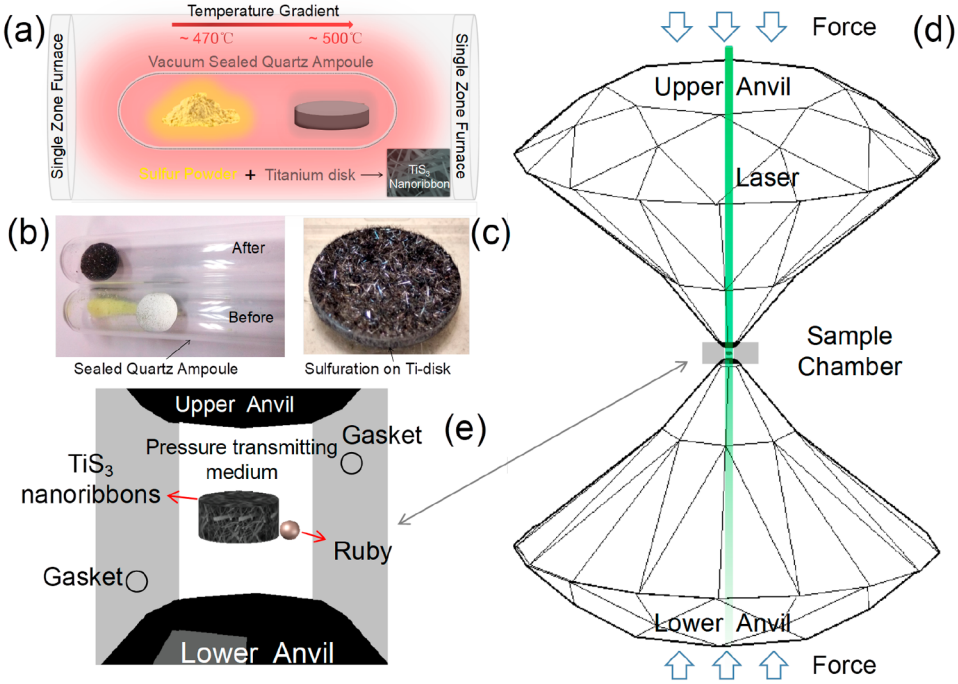


**Figure 2.** (a) Schematic of solid−gas reaction method involved in fabrication of $TiS_3$ nanoribbons. For clarity, optical images of (b) sealed ampules before and after the synthesis process and (c) a zoomed-in view of sulfurated titanium disk are shown. Schematics of (d) diamond and (e) gasket used in the diamond anvil cell are also shown. The schematics are made by using AutoCAD software, version 2020.



https://dx.doi.org/10.1021/acsanm.0c01583
ACS Appl. Nano Mater. 2020, 3, 8794−8802

up to 26 GPa[37] within conclusive phonon modes behavior at high pressure. Kang et al. using *ab initio* calculations on the electronic band structure of $TiS_3$ film suggest its band gap to be independent of the number of layers, stacking order, and vertical strain, and they attribute this result to the absence of charge density redistribution in the interlayer region.[42] Recently a strain-induced dynamical instability in a $TiS_3$ monolayer was obtained from phonon dispersion calculations. It was revealed that $TiS_3$ becomes dynamically unstable for an applied uniaxial tensile strain larger than 6% (8%) along the *a* (*b*)-direction,[43] which is yet to be examined experimentally. The anharmonicity of phonon modes is responsible for various thermal properties such as thermal expansion and thermal conductivity of materials. By investigation of Raman spectra as a function of pressure and temperature independently, complete information about the quasi-harmonic and true anharmonic components of the phonon modes and the implications can be analyzed.[44] In an earlier study,[30] we reported our temperature-dependent Raman spectroscopic studies on $TiS_3$ nanoribbons in the range 88−570 K. Four out-of-plane $A_g$ phonon modes linearly soften (red-shift) with temperature, and the $TiS_3$ compound was found to be stable in this temperature range. However, the pressure-dependent phonon vibrational properties of few-layer $TiS_3$ nanoribbons remain unexplored. Therefore, it is of interest to investigate the effect of high pressure on the vibrational properties of $TiS_3$ to identify the anharmonic phonons and consequently its structural instability. Moreover, the contribution of these phonons to thermal expansion can also be estimated by using high-pressure mode behaviors. To our knowledge, there are no reports of the effect of pressure on vibrational properties of $TiS_3$ nanoribbons or estimation of its thermal expansion by using the phonon spectroscopic results.

In this work, we report pressure-dependent Raman spectroscopic studies of $TiS_3$ nanoribbons synthesized by the direct solid−gas reaction method. TEM studies on the as-synthesized materials suggest a highly crystalline nature of the as-prepared sample.[30] *In situ* high-pressure Raman spectroscopic studies in a diamond anvil cell were performed up to 34 GPa to study the phonon behavior under compression and any possible phase transition(s) at high pressure. Anomalies in the slope of mode frequency, line width, and their Raman intensity in $TiS_3$ nanoribbon are attributed to a possible onset of structural transition at 13 GPa, subsequently resulting in a complete structural phase transition at 43 GPa. Pressure coefficients and mode Grüneisen parameters of the $A_g$ modes were obtained from their Raman spectra. The contribution of these phonons to the thermal expansion across the *a*−*b* plane (along the *c*-axis) is estimated by using our experimental mode Grüneisen parameters. To obtain reliable information about the phase transition and Grüneisen parameter, Raman spectra were measured at close intervals of pressure.

## RESULTS AND DISCUSSION

The fabrication of $TiS_3$ nanoribbons was accomplished by using the solid−gas reaction method (Figure 2a−c). The details on the synthesis are reported in the Experimental Section and our earlier studies.[30,32] A typical schematic of the diamond anvil cell used for high-pressure Raman measurements is depicted in Figure 2d; the close-up view schematic of the sample chamber is shown in Figure 2e to have a better understanding of the sample, ruby, pressure transmitting medium, and gasket position between two anvils.

**Morphological Structure.** The morphology of as-prepared $TiS_3$ materials was investigated by using low- and high-magnification SEM (Figure 3a,b). The SEM micrograph

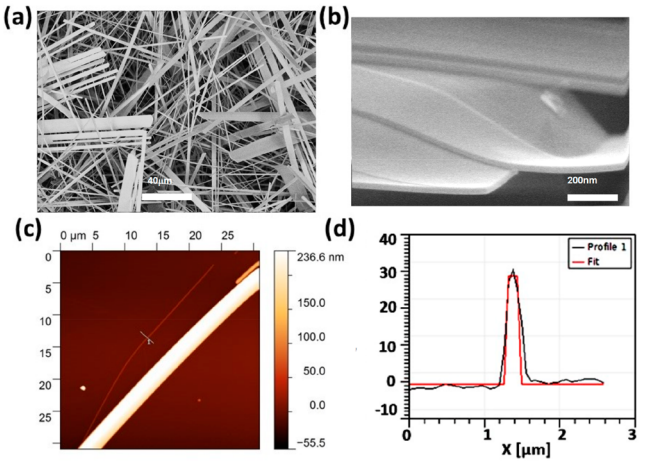


**Figure 3.** Scanning electron microscopy results on the $TiS_3$ nanoribbon: (a) low-magnification SEM image recorded from the $TiS_3$ nanoribbon; (b) highly magnified SEM image of the $TiS_3$ nanoribbon; (c) AFM image and (d) AFM height profile of the $TiS_3$ nanoribbon.

shows the nanoribbons of length 30−80 $\mu$m and width about 2 $\mu$m. The HRTEM image confirms growth of ribbon along a (011) plane with lattice spacing 0.41 nm,[30] in accordance with JCPDS data card no. 00-015-0783. The AFM image and its height profile (Figure 3c,d) indicate the thickness of the nanoribbon is about ∼30 nm, suggesting that each nanoribbon consists of multilayers of $TiS_3$ (∼43 layers).

**High-Pressure Raman Spectroscopy.** At ambient temperature and pressure the crystal structure (space group $P2_1/m$) of $TiS_3$ belongs to the $C_{2h}$ point group with two formula units per unit cell.[45] Factor group analysis suggests that the distribution of Raman-active phonons among different irreducible representations[46] is $\Gamma = 8A_g + 4B_g$. The nonvanishing polarizability tensor corresponding to these Raman modes are[47]

$$A_g = \begin{bmatrix} a & 0 & d \\ 0 & b & 0 \\ d & 0 & c \end{bmatrix} \quad \text{and} \quad B_g = \begin{bmatrix} 0 & e & 0 \\ e & 0 & f \\ 0 & f & 0 \end{bmatrix}$$

The Raman spectrum of the $TiS_3$ nanoribbon recorded at ambient temperature (Figure 4) shows four prominent $A_g$ Raman bands located at 175, 300, 370, and 557 $cm^{-1}$, similar to the number of modes reported earlier.[30] These band positions are obtained by fitting the Raman spectrum to a Lorentzian function. These observed Raman-active phonon modes vibrate along the *c*-axis, perpendicular to the quasi-1D chain. $B_g$ phonon modes involving atomic displacement along the chain (*b*-axis) are weak;[30,45] hence, they are not discernible in the Raman spectrum. The Raman band at 175 $cm^{-1}$ arises due to rigid vibrations of the 1D-$TiS_3$ chain.[31,45] On the other hand, the bands located at 300 $cm^{-1}$ (degenerate band) and 370 $cm^{-1}$ correspond to the internal vibrations of the polyhedral $TiS_6$ unit, and the degenerate band at 557 $cm^{-1}$ arises due to a predominant contribution from the nonbridging S−S pair vibration (diatomic vibration) of the trigonal


https://dx.doi.org/10.1021/acsanm.0c01583
ACS Appl. Nano Mater. 2020, 3, 8794−8802

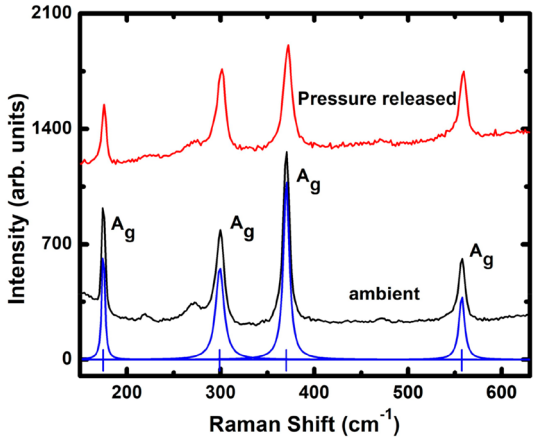


**Figure 4.** Raman spectra of $TiS_3$ nanoribbons at ambient and after complete pressure released in a diamond anvil cell. The deconvoluted individual Raman bands (blue color) are also shown. Blue tick marks locate the calculated prominent Raman bands of the ambient phase. For clarity, the spectra are vertically shifted.

prism.[31,37] For clarity, schematic representations of the motion of atoms for different pressure-sensitive Raman-active phonon modes are represented in Figure 1c. To examine the changes in the Raman spectrum of $TiS_3$ nanoribbon under the influence of high pressure, the Raman spectra were recorded in the DAC at different pressures (Figure 5). At 0.6 GPa, the spectral features are found to be similar to the ambient one (Figure 4). As the pressure is increased, the intensity of Raman bands except that at 557 $cm^{-1}$ reduces and peaks are broadened. Although the rigid band at 175 $cm^{-1}$ survives at high pressure, its intensity reduces significantly and becomes weak at high pressure. The band intensity of the 557 $cm^{-1}$ mode grows as pressure is increased up to ~13 GPa and reduces thereafter up to 34 GPa, the highest pressure of the present studies. In addition, the line width of this band is found to be insensitive to pressure up to ~13 GPa and softens continuously upon further compression. The band located at 484 $cm^{-1}$, close to the highest frequency S−S diatomic vibrational band, has been attributed to the nearly degenerate band at 557 $cm^{-1}$.[37,45] The appearance of this band at high pressure (20−25 GPa) can be considered to be due to their different pressure dependencies. The line-width behavior of Raman bands with pressure will be discussed later. At high pressure, as can be seen in Figure 5b, the 557 $cm^{-1}$ band shifts to lower frequency. Usually, as can be expected, upon compression, the phonon mode frequencies increase as bond lengths involving atomic vibration are reduced. However, sometimes the mode frequency decreases under the influence of pressure, and such modes are known as soft modes.[44] The existence of such soft modes often suggests instability of the crystal lattice, and eventually the system undergoes a structural phase transition. In the present case, the decrease of the 557 $cm^{-1}$ mode frequency with pressure is due to the increase of the S−S bond length possibly due to electron−phonon interaction. Often in 2D materials,[40] the softening of phonon is due to the effect of electron−phonon interaction because of the reduction in interlayer spacing under compression. More evidence of phase transition is noticed from the pressure dependencies of mode frequencies and other spectral parameters such as mode line width and intensity. The spectral parameters are obtained by quantitative analysis of the pressure-dependent Raman spectra by using a Lorentzian

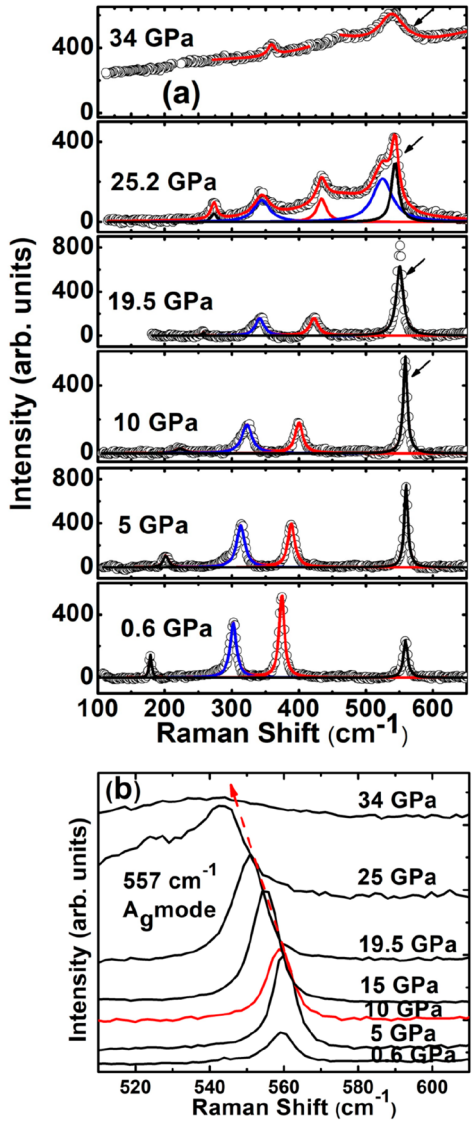


**Figure 5.** (a) Raman spectra of $TiS_3$ nanoribbons at different pressures. Open circles are the experimental data, and solid lines are the fits for individual bands and total fit to the data. Softening of the mode is indicated by arrows. (b) For brevity, the $A_g$ mode at 557 $cm^{-1}$ continues to soften upon increase in pressure above 13 GPa.

function. The pressure evolution of Raman mode frequencies (Figure 6) shows anomalous behavior of these modes around ~13 GPa which can be attributed to the onset of structural transition resulting from structural distortion. Upon increasing pressure, a complete structural transition is evident as discussed later. The theory of mean-field approximation relates the soft phonon with structural transition.[48] The square of the soft phonon mode frequency ($\omega^2$) is related to its transition pressure by the relation $\omega^2 \propto (P - P_c)$, for $P < P_c$, and the soft phonon vanishes as the pressure approaches a transition pressure ($P_c$). The variation of $\omega^2$ as a function of pressure is depicted in Figure 7a. As can be noticed, $\omega^2$ falls linearly up to 34 GPa, the highest pressure covered in the present investigation. In the absence of experimental data above 34 GPa, the fitted parameters obtained from the linear curve fitting of the experimental data were used to extrapolate the mode frequency with respect to pressure in the high-pressure region (>34 GPa), and we found that the 557 $cm^{-1}$ $A_g$ soft


https://dx.doi.org/10.1021/acsanm.0c01583
ACS Appl. Nano Mater. 2020, 3, 8794−8802

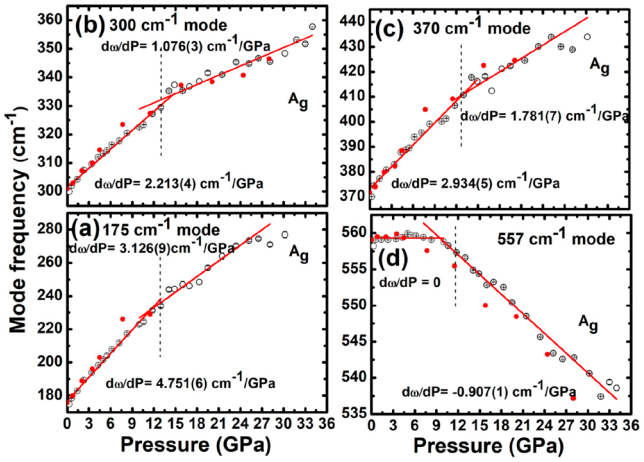


**Figure 6.** Pressure-dependent Raman mode frequencies of $TiS_3$ nanoribbons. Open and solid symbols correspond to data during the compression and decompression cycle, respectively. Solid lines are linear fits to the frequencies. The $A_g$ mode at 557 $cm^{-1}$ softens and undergoes a dramatic change in slope $d\omega/dP$ near 13 GPa. All other $A_g$ modes harden with pressure and exhibit a slope change ~13 GPa, the onset of transition pressure.

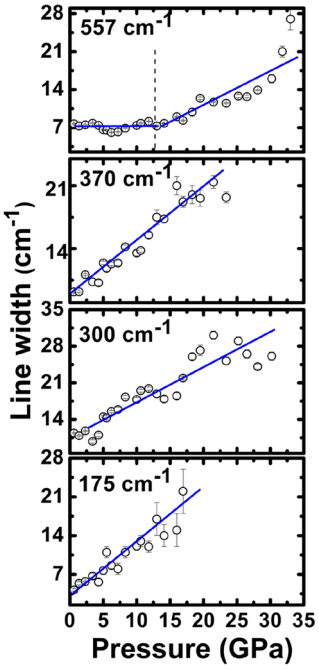


**Figure 8.** Pressure-dependent line widths of Raman bands of $TiS_3$ nanoribbons. Open symbols correspond to the evolution of band line widths during compression. Solid lines are a guide to the eye. Vertical dotted lines show change of slope at the onset of the transition pressure.

mode vanishes at 43 GPa, the expected complete structural transition pressure. It can be mentioned here that first-principles calculations of the strain dependence of phonon dispersion curves of $TiS_3$ monolayer predicted a structural instability[43] at large strain values of 6%−8%. Upon increasing strain up to 6%−8%, we observed imaginary vibrational frequencies at the Γ-point of the reported phonon dispersion curves pointing toward a structural transition,[43] and that theoretically predicted transition is corroborated experimentally in our present HP Raman spectroscopic investigation. The pressure dependencies of the line widths of the observed phonon modes are shown in Figure 8. The line widths of the rigid chain mode at 175 $cm^{-1}$ and internal modes located at 300 and 370 $cm^{-1}$ broaden at high pressure. These internal modes line widths are found to nearly double between 13 and 34 GPa. Upon increasing pressure, the anisotropy of the Ti−S octahedra increases. As a result, the distribution of Ti−S bond lengths is expected to increase. This leads to an increase in the inhomogeneous broadening of these internal vibrations. The broadening of rigid mode and the corresponding decrease in mode intensity with increasing pressure indicate a possibility of growth of static positional disorder.[44,49] On the other hand, the line width of highest frequency band at 557 $cm^{-1}$ is found to be insensitive to pressure up to ~13 GPa, followed by an increasing trend, and thus shows an anomaly around 13 GPa as depicted in Figure 8. The line width of this mode increases by a factor of 4 between 13 and 34 GPa. It can be mentioned here that such an anomaly in the line width of phonons was observed when materials undergo either a structural[50] or an electronic transition ($MoS_2$[40] and $Sb_2Se_3$[51]).

To identify the phase transition in 2D materials, an intensity analysis of Raman mode is useful.[40] This is due to the fact that light couples directly with the polarization in materials and manifests in its intensity.[52] The integrated Raman intensity of the band at 557 $cm^{-1}$ was normalized with respect to that of the band at 300 $cm^{-1}$. The latter band corresponds to the

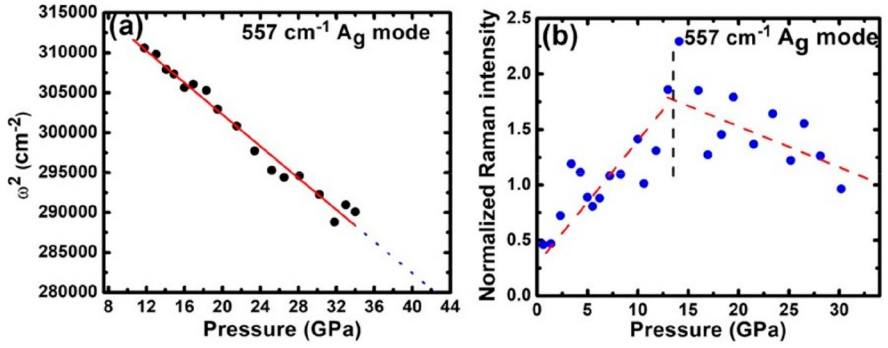


**Figure 7.** (a) Pressure dependence of the square of the Raman-active $A_g$ soft mode frequency. The solid line is a linear fit to the data, and the dotted line corresponds to extrapolated line into the high-pressure field indicating the complete structural phase transition at 43 GPa. (b) Pressure dependencies of normalized integrated intensity of the 557 $cm^{-1}$ mode with respect to that of mode at 300 $cm^{-1}$. The curve drawn through the data point is a guide to the eye. The vertical line shows the anomaly in intensity behavior around the onset of transition pressure, ~13 GPa.



https://dx.doi.org/10.1021/acsanm.0c01583
ACS Appl. Nano Mater. 2020, 3, 8794−8802

Table 1. Pressure Coefficients and Grüneisen Parameters of Raman Modes in the Ambient Phase and High-Pressure Phase[a]

| ambient phase | | | | | | HP phase | |
|---|---|---|---|---|---|---|---|
| mode frequency ($cm^{-1}$) | | | | | | | |
| 0.6 GPa | 300 K | 88 K[b] | P-coefficient ($cm^{-1}$/GPa) | reduced P-coefficient ($GPa^{-1}$) | Grüneisen parameter $\gamma_i$ | P-coefficient ($cm^{-1}$/GPa) | reduced P-coefficient ($GPa^{-1}$) |
| 178 ($A_g$) | 175 | 177 | 4.75(4) | 0.027142 | 1.3571 | 3.12(8) | 0.017828 |
| 302 ($A_g$) | 300 | 302 | 2.21(9) | 0.007366 | 0.3683 | 1.07(7) | 0.003566 |
| 374 ($A_g$) | 370 | 371 | 2.93(7) | 0.007918 | 0.3959 | 1.78(1) | 0.004811 |
| 559 ($A_g$) | 557 | 560 | 0[c] | | | −0.91(3) | −0.001634 |

[a]Numbers in the parentheses are the standard errors in the least significant digit. [b]Reference 30. [c]Error larger than the slope value is considered as zero.

internal vibrations of the $TiS_6$ octahedron, which persists over the entire pressure range of this study and exhibits a slight change in its intensity upon compression. The pressure dependence of the normalized intensity of the 557 $cm^{-1}$ mode is shown in Figure 7b. One can notice that the intensity increases up to 13 GPa and subsequently falls beyond this pressure. Hence, the observed anomaly in the mode intensity around 13 GPa is similar to the onset of transition pressure as noticed from Figures 6 and 8 and further corroborates that the $TiS_3$ nanoribbons undergo a pressure-induced structural transition which begins at ∼13 GPa. The Raman spectra were also recorded in the pressure-released cycle, and their peak positions with pressure follow the same trend as observed in the compression cycle is shown in Figure 5. After complete pressure release, the Raman spectrum is found to be reversible and matches with the ambient spectrum obtained from the pristine $TiS_3$ nanoribbon sample as shown in Figure 4. This suggests that the pressure-induced structural transition of $TiS_3$ nanoribbons is completely reversible.

The pressure coefficients of Raman bands were obtained by linear fit to $\omega_i$ vs $P$ curves in ambient and HP phases (Figure 6). The low-frequency $A_g$ mode which is attributed to the rigid chain vibration has a large pressure dependency, while the 557 $cm^{-1}$ mode is insensitive to pressure (slope ∼0) in the ambient phase. Frequencies of modes at 175, 300, and 370 $cm^{-1}$ increase upon compression and follow normal hardening behavior, whereas the highest frequency mode located at 557 $cm^{-1}$ becomes almost constant in the ambient phase below 13 GPa. The pressure dependencies of modes in the HP phase (13−34 GPa) are found to be less compared to those of the ambient phase. The pressure coefficient of the band at 557 $cm^{-1}$ is found to be negative (Table 1). The reduced slopes $\frac{1}{\omega_i}\frac{\partial \omega_i}{\partial P}$ of phonon modes, which essentially represent the bond strength of phonon vibrational modes[44] in both phases, were obtained (Table 1). In the ambient phase, the reduced slope of the 175 $cm^{-1}$ rigid chain mode is larger than the others, indicating that this mode is more sensitive to pressure and gets easily compressed and deformed, whereas a low value of reduced slopes for the 300 and 370 $cm^{-1}$ internal modes suggests that these vibrations are comparatively less sensitive to pressure. Because the normalized slopes of modes in HP phase are lower than those in the ambient phase (Table 1), the mode vibrations in the HP phase are less influenced by compression, and the bonds involving these atomic vibrations are stiffer. The band at 557 $cm^{-1}$ has a moderate value of negative reduced slope pointing toward its contribution to negative thermal expansion in the HP phase. Mode Grüneisen parameters of $A_g$ modes which exhibit out-of-plane vibration (along $c$-axis) are calculated by using the relationship[44] $\gamma_i = (\omega_i \chi_c)^{-1}\frac{\partial \omega_i}{\partial P}$, where $\chi_c$ is the axial compressibility along the $c$-axis. Using the reported $\chi_c^{-1}$ = 50 GPa,[37] $\gamma_i$ values were calculated by using our experimental pressure dependencies of mode frequencies. Mode Grüneisen parameters $\gamma_i$ of $A_g$ modes of the ambient phase are listed in Table 1. A larger value of $\gamma_i$ of the rigid mode 175 $cm^{-1}$ implies more contribution to the thermal expansion coefficient. These microscopic parameters $\gamma_i$ are key input for obtaining thermal properties such as the specific heat and thermal expansion coefficient of materials, as described below.

The contribution of the observed $A_g$ phonon modes to thermal expansion coefficient $\alpha$ of the $TiS_3$ nanoribbon can be estimated by using $\alpha = (\gamma_{av} C_v)/(3V_m \chi_c^{-1})$, where $C_v$ is the molar specific heat at constant volume, $\gamma_{av}$ is the average Grüneisen parameter, $V_m$ is the molar volume, and $\chi_c^{-1}$ is the axial compressibility along the $c$-axis. Using Einstein's specific heat, $C_i = R[y_i^2 \exp(y_i)]/[\exp(y_i) - 1]^2$, where $y_i = \hbar\omega_i/k_B T$ and $R$ is the gas constant, the total specific heat $C_v$ can be obtained ($i$ = 1−4), and $\gamma_{av}$ is defined as $\gamma_{av} = 1/2(\sum p_i C_i \gamma_i)/C_v$, where $p_i$ is the degeneracy of phonon at Brillouin zone center. Using the unit cell volume, the molar volume is calculated as $4.439 \times 10^{-5}$ $m^3$/mol; the reported $\chi_c^{-1}$ value is taken as 50 GPa,[37] and considering our experimental mode Grüneisen parameters, the linear thermal expansion along the $c$-axis at 300 K is estimated as $\alpha = 1.321 \times 10^{-6}$ $K^{-1}$, which is found to be of the same order of magnitude as the one reported in $MoS_2$.[53]

As mentioned earlier, the change in mode frequency due to the effect of temperature has two contributions. One is due to the phonon−phonon interaction at constant volume known as the intrinsic anharmonic contribution (explicit), and other one is an implicit contribution that solely depends on the lattice volume change. The latter implicit quasi-harmonic contribution is obtained from pressure dependence of mode frequency and enables one to infer the explicit, true anharmonicity of phonon modes. The Raman mode frequencies of $TiS_3$ observed by compression at 0.6 GPa and cooling to 88 K[30] are listed in Table 1. Inspection of these Raman shift values indicates that several of the mode frequencies obtained by way of compression is nearly the same as that obtained by volume contraction achieved by cooling. This suggests that most of the mode frequencies behavior with temperature is mainly due to the quasi-harmonic contribution (caused by only change in lattice volume). However, the mode at 370 $cm^{-1}$ has a significant difference in its Raman shift with temperature and pressure, indicating the highly anharmonic nature which arises from the phonon−phonon interaction. The present phonon spectral studies at high pressure provide insight into the role of several $A_g$ phonons in the structural phase transition and thermal expansion in $TiS_3$ nanoribbons. Our experimental


https://dx.doi.org/10.1021/acsanm.0c01583
ACS Appl. Nano Mater. 2020, 3, 8794−8802

finding is consistent with the theoretically predicted structural phase transition from phonon dispersion calculations.

## CONCLUSIONS

In conclusion, we report pressure-dependent Raman spectroscopic studies of out-of-plane $A_g$ phonons in titanium trisulfide nanoribbons prepared by the direct solid−gas reaction method and infer their cross-plane thermal expansion coefficient. Out of four prominent observed $A_g$ modes, the phonon modes at 175, 300, and 370 $cm^{-1}$ show a blue-shift upon compression while that located at 557 $cm^{-1}$exhibits softening about 13 GPa. Anomalies in phonon mode frequencies and excessive broadening in line width of the soft phonon about 13 GPa are attributed to the onset of a structural transition. The complete structural phase transition at 43 GPa is observed from extrapolation, consistent with recent reported *ab initio* theoretical predictions. The first-order pressure coefficients of $A_g$ modes are found to lie in the range 0.3−1.5 $cm^{-1}$/GPa. The experimental mode Grüneisen parameter of the 175 $cm^{-1}$ vibrational $A_g$ mode is large and sensitive to pressure. Using these mode Grüneisen parameters, we estimated cross-plane thermal expansion at 300 K to be 1.32 × $10^{-6}$ $K^{-1}$. The structural change in the $TiS_3$ nanoribbon under compression is recovered in the pressure release cycle. The observed results can be crucial in calibration and correction of performance of next-generation $TiS_3$-based nanoelectronics and optical devices under extreme stress conditions.

## EXPERIMENTAL SECTION

Titanium trisulfide layers have been obtained by direct sulfuration of a Ti disc (diameter 10 mm) in a vacuum-sealed ampule at 550 °C for 20 h (see the schematic in Figure 2a−c). The used Ti discs were etched in $HNO_3$:HF (30:4 wt %) for 1 min, followed by washed in distilled water, and subsequently dipped in ethanol. The heating rate was 0.4 ± 0.05 °C/min, and the cooling took place in ambient conditions. The detailed synthesis procedure for $TiS_3$ nanoribbons is described in our earlier reports.[30,32] The microstructure of the materials was investigated by using a scanning electron microscope. The thickness of the nanoribbon was characterized by using an atomic force microscope (ICON system, Bruker, Santa Barbara, CA) operated in contact mode. *In situ* high-pressure Raman spectroscopic measurements were performed by using a compact, symmetric diamond anvil cell (DAC) with diamonds of culet diameter 500 μm. Raman spectra were recorded by using a micro-Raman spectrometer (Renishaw inVia) operated in the backscattering configuration. A 514.5 nm line from an Ar-ion laser with an output power of ∼0.4 mW is used for excitation of the sample. A few flakes of $TiS_3$ sample were loaded into a 200 μm hole of a preindented stainless-steel gasket in the DAC. A 4:1 methanol−ethanol mixture was used as the pressure transmitting medium and ruby was loaded along with the sample as a pressure calibrant (see the schematic in Figure 2d,e). Measurements were performed up to ∼34 GPa, covering the wavenumber range 100−650 $cm^{-1}$. Raman spectra were also recorded during the pressure-reducing cycle. The pressure transmitting medium is quasi-hydrostatic up to 10 GPa, and beyond this pressure the experimental results can be influenced by uniaxial pressure.[49,54] The spectra were analyzed by Lorentzian line shapes using Peak Fit software (JANDEL).

## AUTHOR INFORMATION


### Corresponding Author

**Dattatray J. Late** − *Centre for Nanoscience & Nanotechnology, Amity University Maharashtra, Panvel, Maharashtra 410206, India;* orcid.org/0000-0003-3007-7220; Email: datta099@gmail.com, djlate@mum.amity.edu

### Authors

**K. K. Mishra** − *Department of Physics and Institute for Functional Nanomaterials, University of Puerto Rico, San Juan, Puerto Rico 00931*

**T. R. Ravindran** − *HBNI, Materials Science Group, Indira Gandhi Centre for Atomic Research, Kalpakkam 603102, India;* orcid.org/0000-0002-4534-8487

**Joshua O. Island** − *Kavli Institute of Nanoscience, Delft University of Technology, 2628 CJ Delft, Netherlands;* orcid.org/0000-0002-6074-9414

**Eduardo Flores** − *FINDER-Group, Instituto de Micro y Nanotecnología, IMN-CNM, CSIC (CEI UAM+CSIC), E-28760 Madrid, Spain;* orcid.org/0000-0003-4769-0873

**Jose Ramon Ares** − *Materials of Interest in Renewable Energies Group (MIRE Group), Departamento de Física de Materiales, Universidad Autónoma de Madrid, UAM, 28049 Madrid, Spain;* orcid.org/0000-0001-5238-1800

**Carlos Sanchez** − *Materials of Interest in Renewable Energies Group (MIRE Group), Departamento de Física de Materiales, Universidad Autónoma de Madrid, UAM, 28049 Madrid, Spain;* orcid.org/0000-0001-9816-4537

**Isabel J. Ferrer** − *Materials of Interest in Renewable Energies Group (MIRE Group), Departamento de Física de Materiales, Universidad Autónoma de Madrid, UAM, 28049 Madrid, Spain;* orcid.org/0000-0003-2125-5865

**Herre S. J. van der Zant** − *Kavli Institute of Nanoscience, Delft University of Technology, 2628 CJ Delft, Netherlands;* orcid.org/0000-0002-5385-0282

**Amit Pawbake** − *J. Heyrovský Institute of Physical Chemistry, Czech Academy of Sciences, 182 23 Prague, Czech Republic;* orcid.org/0000-0002-6345-489X

**R. Kanawade** − *Department of Physics, Savitribai Phule Pune University, Pune 411008, India*

**Andres Castellanos-Gomez** − *Materials Science Factory, Instituto de Ciencia de Materiales de Madrid, Consejo Superior de Investigaciones Científicas, 28049 Madrid, Spain;* orcid.org/0000-0002-3384-3405

Complete contact information is available at: https://pubs.acs.org/10.1021/acsanm.0c01583


### Author Contributions

D.J.L. and A.C.-G. conceptualized this project. J.O.I., E.F., J.R.A., C.S., I.J.F., H.S.J.Z.A.P., A.C.-G., and D.J.L. prepared and characterized the materials. K.K.M. and T.R.R. performed the pressure dependence Raman spectroscopy measurements of the $TiS_3$ nanoribbon and processed the data. A.P. and K.K.M. prepared the all schematic representations. All authors analyzed and discussed the data. K.K.M. and D.J.L. wrote the first draft of the manuscript, with all authors commenting and editing the manuscript.

### Notes

The authors declare no competing financial interest.

## ACKNOWLEDGMENTS

D.J.L. thanks the Science and Engineering Research Board (SERB), Government of India, for funding. K.K.M. thanks Prof. R. S. Katiyar, University of Puerto Rico, for encouragement. A.P. acknowledges a grant (CZ.02.2.69/0.0/0.0/16_027/0008355) for postdoc funding.



https://dx.doi.org/10.1021/acsanm.0c01583
ACS Appl. Nano Mater. 2020, 3, 8794−8802

## REFERENCES


(1) Li, H.; Zhang, Q.; Yap, C. C. R.; Tay, B. K.; Edwin, T. H. T.; Olivier, A.; Baillargeat, D. From Bulk to Monolayer $MoS_2$: Evolution of Raman Scattering. *Adv. Funct. Mater.* **2012**, *22*, 1385−1390.

(2) Pawbake, A. S.; Date, A.; Jadkar, S. R.; Late, D. J. Temperature Dependent Raman Spectroscopy and Sensing Behavior of Few Layer $SnSe_2$ Nanosheets. *Chemistry Select* **2016**, *1*, 5380−5387.

(3) Kannan, P. K.; Late, D. J.; Morgan, H.; Rout, C. S. Recent Developments in 2D Layered Inorganic Nanomaterials for Sensing. *Nanoscale* **2015**, *7*, 13293−13312.

(4) Ramakrishna Matte, H. S. S.; Gomathi, A.; Manna, A. K.; Late, D. J.; Datta, R.; Pati, S. K.; Rao, C. N. R. $MoS_2$ and $WS_2$ Analogues of Graphene. *Angew. Chem., Int. Ed.* **2010**, *49*, 4059−4062.

(5) Wang, Q. H.; Kalantar-Zadeh, K.; Kis, A.; Coleman, J. N.; Strano, M. S. Electronics and Optoelectronics of Two-Dimensional Transition Metal Dichalcogenides. *Nat. Nanotechnol.* **2012**, *7*, 699−712.

(6) Bhimanapati, G. R.; et al. Recent Advances in Two-Dimensional Materials Beyond Graphene. *ACS Nano* **2015**, *9*, 11509−11539.

(7) Akinwande, D.; Petrone, N.; Hone, J. Two-Dimensional Flexible Nanoelectronics. *Nat. Commun.* **2014**, *5*, 1−12.

(8) Huo, N.; Yang, S.; Wei, Z.; Li, S. S.; Xia, J. B.; Li, J. Photoresponsive and Gas Sensing Field-Effect Transistors Based on Multilayer $WS_2$ Nanoflakes. *Sci. Rep.* **2015**, *4*, 52091−52099.

(9) Late, D. J.; Huang, Y. K.; Liu, B.; Acharya, J.; Shirodkar, S. N.; Luo, J.; Yan, A.; Charles, D.; Waghmare, U. V.; Dravid, V. P.; Rao, C.N. R. Sensing Behavior of Atomically Thin-Layered $MoS_2$Transistors. *ACS Nano* **2013**, *7*, 4879−4891.

(10) Yin, Z.; Li, H.; Li, H.; Jiang, L.; Shi, Y.; Sun, Y.; Lu, G.; Zhang, Q.; Chen, X.; Zhang, H. Single-Layer $MoS_2$ Phototransistors. *ACS Nano* **2012**, *6*, 74−80.

(11) Lopez-Sanchez, O.; Lembke, D.; Kayci, M.; Radenovic, A.; Kis, A. Ultrasensitive Photodetectors Based on Monolayer $MoS_2$. *Nat. Nanotechnol.* **2013**, *8*, 497−501.

(12) Qiu, H.; Pan, L.; Yao, Z.; Li, J.; Shi, Y.; Wang, X. Electrical Characterization of Back-gated Bi-layer $MoS_2$ Field-Effect Transistors and the Effect of Ambient on their Performances. *Appl. Phys. Lett.* **2012**, *100*, 1231041−1231043.

(13) Late, D. J.; Shaikh, P. A.; Khare, R.; Kashid, R. V.; Chaudhary, M.; More, M. A.; Ogale, S. B. Pulsed Laser-Deposited $MoS_2$Thin Films on W and Si: Field Emission and Photoresponse Studies. *ACS Appl. Mater. Interfaces* **2014**, *6*, 15881−15888.

(14) Pawbake, A. S.; Waykar, R. G.; Late, D. J.; Jadkar, S. R. Highly Transparent Wafer-Scale Synthesis of Crystalline $WS_2$ Nanoparticle Thin Film for Photodetector and Humidity-Sensing Applications. *ACS Appl. Mater. Interfaces* **2016**, *8*, 3359−3365.

(15) Buscema, M.; Island, J. O.; Groenendijk, D. J.; Blanter, S. I.; Steele, G. A.; van der Zant, H. S.; Castellanos-Gomez, A. Photocurrent Generation with Two-Dimensional van der waals Semiconductors. *Chem. Soc. Rev.* **2015**, *44*, 3691−3718.

(16) Lee, G. H.; Cui, X.; Kim, Y. D.; Arefe, G.; Zhang, X.; Lee, C. H.; Ye, F.; Watanabe, K.; Taniguchi, T.; Kim, P.; Hone, J. Highly Stable Dual-gated $MoS_2$Transistors Encapsulated by Hexagonal Boron Nitride with Gate-Controllable Contact Resistance and Threshold Voltage. *ACS Nano* **2015**, *9*, 7019−7026.

(17) Das, S.; Chen, H. Y.; Penumatcha, A. V.; Appenzeller, J. High Performance Multilayer $MoS_2$ Transistors with Scandium Contacts. *Nano Lett.* **2013**, *13*, 100−105.

(18) Wu, W.; De, D.; Chang, S. C.; Wang, Y.; Peng, H.; Bao, J.; Pei, S. S. High Mobility and High on/off ratio Field-effect Transistors Based on Chemical Vapor Deposited Single-Crystal $MoS_2$ Grains. *Appl. Phys. Lett.* **2013**, *102*, 142106.

(19) Wang, H.; Yu, L.; Lee, Y. H.; Shi, Y.; Hsu, A.; Chin, M. L.; Li, L. J.; Dubey, M.; Kong, J.; Palacios, T. Integrated Circuits Based on Bilayer $MoS_2$Transistors. *Nano Lett.* **2012**, *12*, 4674−4680.

(20) Late, D. J.; Liu, B.; Matte, H. S. S. R.; Dravid, V. P.; Rao, C. N. R. Hysteresis in single-layer $MoS_2$ field effect transistors. *ACS Nano* **2012**, *6*, 5635−5641.

(21) Groenendijk, D. J.; Buscema, M.; Steele, G. A.; Michaelis de Vasconcellos, S.; Bratschitsch, R.; van der Zant, H. S.; Castellanos-Gomez, A. Photovoltaic and Photothermoelectric Effect in a Double-gated $WSe_2$ Device. *Nano Lett.* **2014**, *14*, 5846−5852.

(22) Pospischil, A.; Furchi, M. M.; Mueller, T. Solar-Energy Conversion and Light Emission in an Atomic Monolayer *p-n* Diode. *Nat. Nanotechnol.* **2014**, *9*, 257−261.

(23) Late, D. J.; Rout, S. C.; Chakravarty, D.; Ratha, D. Emerging Energy Applications of Two-Dimensional Layered Materials. *Can. Chem. Trans.* **2015**, *3*, 118−157.

(24) Kashid, R. V.; Late, D. J.; Chou, S. S.; Huang, Y. K.; De, M.; Joag, D. S.; More, M. A.; Dravid, V. P. Enhanced Field-Emission Behavior of Layered $MoS_2$ Sheets. *Small* **2013**, *9*, 2730−2734.

(25) Rout, C. S.; Joshi, P. D.; Kashid, R. V.; Joag, D. S.; More, M. A.; Simbeck, A. J.; Washington, M.; Nayak, S. K.; Late, D. J. Superior Field Emission Properties of Layered $WS_2$-RGO Nanocomposites. *Sci. Rep.* **2013**, *3*, 32821−32828.

(26) Suryawanshi, S. R.; More, M. A.; Late, D. J. Laser Exfoliation of 2D Black Phosphorus Nanosheets and Their Application as a Field Emitter. *RSC Adv.* **2016**, *6*, 112103−112108.

(27) Suryawanshi, S. R.; Pawbake, A. S.; Pawar, M. S.; Jadkar, S. R.; More, M. A.; Late, D. J. Enhanced Field Emission Behavior of Layered $MoSe_2$. *Mater. Res. Express* **2016**, *3*, 035003.

(28) Lipatov, A.; Wilson, P. M.; Shekhirev, M.; Teeter, J. D.; Netusil, R.; Sinitskii, A. Few-Layered Titanium Trisulfide ($TiS_3$) Field-Effect Transistors. *Nanoscale* **2015**, *7*, 12291−12296.

(29) Island, J. O.; Buscema, M.; Barawi, M.; Clamagirand, J. M.; Ares, J. R.; Sánchez, C.; Ferrer, I. J.; Steele, G. A.; van der Zant, H. S.; Castellanos-Gomez, A. Ultrahigh Photoresponse of Few-Layer $TiS_3$ Nanoribbon Transistors. *Adv. Opt. Mater.* **2014**, *2*, 641−645.

(30) Pawbake, A. S.; Island, J. O.; Flores, E.; Ares, J. R.; Sanchez, C.; Ferrer, I. J.; Jadkar, S. R.; Van Der Zant, H. S.; Castellanos-Gomez, A.; Late, D. J. Temperature-Dependent Raman Spectroscopy of Titanium Trisulfide ($TiS_3$) Nanoribbons and Nanosheets. *ACS Appl. Mater. Interfaces* **2015**, *7*, 24185−24190.

(31) Wieting, T. J.; Grisel, A.; Levy, F. Lattice Dynamical STudy of the Low-Dimensional Type B Compounds $TiS_3$, $HfSe_3$ and $ZrTe_3$. *Physica B+C* **1981**, *105*, 366−369.

(32) Island, J. O.; Barawi, M.; Biele, R.; Almazan, A.; Clamagirand, J. M.; Ares, J. R.; Sanchez, C.; van der Zant, H. S. J.; Alvarez, J. V.; D'Agosta, R.; Ferrer, I. J.; Castellanos-Gomez, A. $TiS_3$ Transistors with Tailored Morphology and Electrical Properties. *Adv. Mater.* **2015**, *27*, 2595−2601.

(33) Dai, J.; Zeng, X. C. Titanium Trisulfide Monolayer: Theoretical Prediction of a New Direct-gap Semiconductor with High and Anisotropic Carrier Mobility. *Angew. Chem., Int. Ed.* **2015**, *54*, 7572−7576.

(34) Island, J. O.; Biele, R.; Barawi, M.; Clamagirand, J. M.; Ares, J. R.; Sánchez, C.; Van Der Zant, H. S.; Ferrer, I. J.; D'Agosta, R.; Castellanos-Gomez, A. Titanium Trisulfide ($TiS_3$): a 2D Semiconductor with Quasi-1D Optical and Electronic Properties. *Sci. Rep.* **2016**, *6*, 222141−222147.

(35) Lipatov, A.; Wilson, P. M.; Shekhirev, M.; Teeter, J. D.; Netusil, R.; Sinitskii, A. Few-Layered Titanium Trisulfide ($TiS_3$) Field-Effect Transistors. *Nanoscale* **2015**, *7*, 12291−12296.

(36) Molina-Mendoza, A. J.; Island, J. O.; Paz, W. S.; Clamagirand, J. M.; Ares, J. R.; Flores, E.; Leardini, F.; Sanchez, C.; Agrait, N.; Rubio-Bollinger, G.; van der Zant, H. S. J.; Ferrer, I. J.; Palacios, J. J.; Castellanos-Gomez, A. High Current Density Electrical Breakdown of $TiS_3$ Nanoribbon-Based Field-Effect Transistors. *Adv. Funct. Mater.* **2017**, *27*, 1605647.

(37) Wu, K.; Torun, E.; Sahin, H.; Chen, B.; Fan, X.; Pant, A.; Wright, D. P.; Aoki, T.; Peeters, F. M.; Soignard, E.; Tongay, S. Unusual Lattice Vibration Characteristics in Whiskers of the Pseudo-One-Dimensional Titanium Trisulfide $TiS_3$. *Nat. Commun.* **2016**, *7*, 129521−129527.

(38) Island, J. O; Molina-Mendoza, A. J; Barawi, M.; Biele, R.; Flores, E.; Clamagirand, J. M; Ares, J. R; Sanchez, C.; van der Zant, H. S J; D'Agosta, R.; Ferrer, I. J; Castellanos-Gomez, A. Electronics and




https://dx.doi.org/10.1021/acsanm.0c01583
ACS Appl. Nano Mater. 2020, 3, 8794−8802

Optoelectronics of Quasi-1D Layered Transition Metal Trichalcogenides. *2D Mater.* **2017**, *4*, 022003.
(39) Mishra, K. K.; Ghosh, S.; Ravindran, T. R.; Amirthapandian, S.; Kamruddin, M. Thermal Conductivity and Pressure-Dependent Raman Studies of Vertical Graphene Nanosheets. *J. Phys. Chem. C* **2016**, *120*, 25092−25100.
(40) Nayak, A. P.; Bhattacharyya, S.; Zhu, J.; Liu, J.; Wu, X.; Pandey, T.; Jin, C.; Singh, A. K.; Akinwande, D.; Lin, J. F. Pressure-Induced Semiconducting to Metallic Transition in Multilayered Molybdenum Disulphide. *Nat. Commun.* **2014**, *5*, 37311−37319.
(41) Clark, S. M.; Jeon, K. J.; Chen, J. Y.; Yoo, C. S. Few-layer Graphene Under High Pressure: Raman and X-ray Diffraction Studies. *Solid State Commun.* **2013**, *154*, 15−18.
(42) Kang, J.; Wang, L. W. Robust Band Gap of $TiS_3$ Nanofilms. *Phys. Chem. Chem. Phys.* **2016**, *18*, 14805−14809.
(43) Aierken, Y.; Çakır, D.; Peeters, F. M. Strain Enhancement of Acoustic Phonon Limited Mobility in Monolayer $TiS_3$. *Phys. Chem. Chem. Phys.* **2016**, *18*, 14434−14441.
(44) Mishra, K. K.; Chandra, S.; Salke, N. P.; Achary, S. N.; Tyagi, A. K.; Rao, R. Soft modes and anharmonicity in $H_3[Co(CN)_6]$: Raman Spectroscopy and First-Principles Calculations. *Phys. Rev. B: Condens. Matter Mater. Phys.* **2015**, *92*, 1341121−1341129.
(45) Gard, P.; Cruege, F.; Sourisseau, C.; Gorochov, O. Single-Crystal Micro-Raman Studies of $ZrS_3$, $TiS_3$ and Several $Zr_{1-x}Ti_xS_3$ Compounds ($0 < x \leqslant 0.33$). *J. Raman Spectrosc.* **1986**, *17*, 283−288.
(46) Osada, K.; Bae, S.; Tanaka, M.; Raebiger, H.; Shudo, K.; Suzuki, T. Phonon Properties of Few-Layer Crystals of Quasi-One-Dimensional $ZrS_3$ and $ZrSe_3$. *J. Phys. Chem. C* **2016**, *120*, 4653−4659.
(47) Loudon, R. The Raman Effect in Crystals. *Adv. Phys.* **1964**, *13*, 423−482.
(48) Cochran, W. Crystal Stability and the Theory of Ferroelectricity. *Phys. Rev. Lett.* **1959**, *3*, 412−414.
(49) Mishra, K. K.; Achary, S. N.; Chandra, S.; Ravindran, T. R.; Sinha, A. K.; Singh, M. N.; Tyagi, A. K. Structural and Thermal Properties of $BaTe_2O_6$: Combined Variable-Temperature Synchrotron X-ray Diffraction Raman Spectroscopy and *ab* Initio Calculations. *Inorg. Chem.* **2016**, *55*, 8994−9005.
(50) Mishra, K. K.; Satya, A. T.; Bharathi, A.; Sivasubramanian, V.; Murthy, V. R. K.; Arora, A. K. Vibrational, Magnetic and Dielectric Behavior of *La*-Substituted $BiFeO_3$-$PbTiO_3$. *J. Appl. Phys.* **2011**, *110*, 123529.
(51) Bera, A.; Pal, K.; Muthu, D. V. S.; Sen, S.; Guptasarma, P.; Waghmare, U. V.; Sood, A. K. Sharp Raman Anomalies and Broken Adiabaticity at a Pressure Induced Transition from Band to Topological Insulator in $Sb_2Se_3$. *Phys. Rev. Lett.* **2013**, *110*, 107401−107405.
(52) Weinstine, B. A.; Zallen, R. In *Topics in Applied Physics*; Cardona, M., Guntherodt, G., Eds.; Springer-Verlag: Berlin, 1984; Vol. *IV*, Chapter 8, pp 463−527.
(53) Gan, C. K.; Liu, Y. Y. F. Direct Calculation of the Linear Thermal Expansion Coefficients of $MoS_2$ via Symmetry-Preserving Deformations. *Phys. Rev. B: Condens. Matter Mater. Phys.* **2016**, *94*, 1343031−1343036.
(54) Klotz, S; Chervin, J-C; Munsch, P; Le Marchand, G Hydrostatic Limits of 11 Pressure Transmitting Media. *J. Phys. D: Appl. Phys.* **2009**, *42*, 0754131−0754137.
(55) Momma, K.; Izumi, F. VESTA 3 for Three-Dimensional Visualization of Crystal, Volumetric and Morphology Data. *J. Appl. Crystallogr.* **2011**, *44*, 1272−1276.


https://dx.doi.org/10.1021/acsanm.0c01583
*ACS Appl. Nano Mater.* 2020, 3, 8794−8802